



# Serial macromolecular crystallography at ALBA Synchrotron Light Source

Jose M. Martin-Garcia,<sup>a,b\*</sup> Sabine Botha,<sup>c</sup> Hao Hu,<sup>c</sup> Rebecca Jernigan,<sup>a</sup> Albert Castellví,<sup>d</sup> Stella Lisova,<sup>c</sup> Fernando Gil,<sup>e</sup> Barbara Calisto,<sup>e</sup> Isidro Crespo,<sup>e</sup> Shatabdi Roy-Chowdhury,<sup>a</sup> Alice Grieco,<sup>b</sup> Gihan Ketawala,<sup>a</sup> Uwe Weierstall,<sup>a,c</sup> John Spence,<sup>a,c</sup> Petra Fromme,<sup>a</sup> Nadia Zatsepin,<sup>a,c,f</sup> Dirk Roeland Boer<sup>e\*</sup> and Xavi Carpena<sup>e\*</sup>

Received 22 November 2021

Accepted 3 March 2022

Edited by R. W. Strange, University of Essex, United Kingdom

**Keywords:** serial synchrotron crystallography; viscous jet; LCP; microcrystal; ALBA; XALOC.

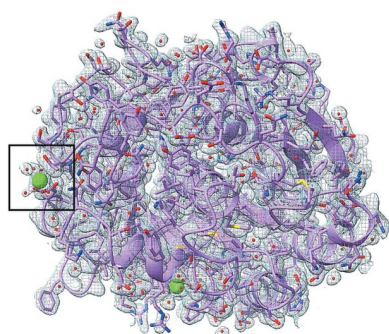
**Supporting information:** this article has supporting information at journals.iucr.org/s

<sup>a</sup>Center for Applied Structural Discovery, Biodesign Institute, Arizona State University, Tempe, AZ, USA, <sup>b</sup>Department of Crystallography and Structural Biology, Institute of Physical Chemistry Rocasolano, Spanish National Research Council (CSIC), Madrid, Spain, <sup>c</sup>Department of Physics, Arizona State University, Tempe, AZ, USA, <sup>d</sup>Molecular Biology Institute of Barcelona, CSIC, Barcelona, Spain, <sup>e</sup>ALBA Synchrotron, Cerdanyola del Vallès, Barcelona, Spain, and <sup>f</sup>ARC Centre of Excellence in Advance Molecular Physics, La Trobe Institute for Molecular Sciencemaging, Department of Chemistry and Physics, La Trobe University, Melbourne, Australia. \*Correspondence e-mail: jmmartin@iqfr.csic.es, rboer@cells.es, xcarpena@cells.es

The increase in successful adaptations of serial crystallography at synchrotron radiation sources continues. To date, the number of serial synchrotron crystallography (SSX) experiments has grown exponentially, with over 40 experiments reported so far. In this work, we report the first SSX experiments with viscous jets conducted at ALBA beamline BL13-XALOC. Small crystals (15–30 µm) of five soluble proteins (lysozyme, proteinase K, phycocyanin, insulin and  $\alpha$ -spectrin-SH3 domain) were suspended in lipidic cubic phase (LCP) and delivered to the X-ray beam with a high-viscosity injector developed at Arizona State University. Complete data sets were collected from all proteins and their high-resolution structures determined. The high quality of the diffraction data collected from all five samples, and the lack of specific radiation damage in the structures obtained in this study, confirm that the current capabilities at the beamline enables atomic resolution determination of protein structures from microcrystals as small as 15 µm using viscous jets at room temperature. Thus, BL13-XALOC can provide a feasible alternative to X-ray free-electron lasers when determining snapshots of macromolecular structures.

## 1. Introduction

There are currently only five X-ray free-electron laser (XFEL) beamlines available worldwide for high-resolution macromolecular crystallography (MX). These scarce resources continue to be in high demand for complex serial femtosecond crystallography (SFX) experiments at XFELs. Meanwhile, the continuous developments in hardware at modern synchrotrons, including faster detectors and brighter beams, have made standard synchrotron beamlines an attractive alternative for performing serial crystallography experiments. Although the vast majority of routine MX experiments are still performed *via* the oscillation method using monochromatic X-ray beams, there has been an increasing trend to use the serial synchrotron crystallography (SSX) approach to solve protein crystal structures from previously intractable crystals of a few micrometres in size. As of February 2022, over 40 SSX experiments were conducted at synchrotrons using exposure times of a few milliseconds (see review article by Martin-Garcia, 2021). To date, almost every one of the third and fourth-generation synchrotrons have at least one MX



OPEN ACCESS

Published under a CC BY 4.0 licence

beamline that may be used for serial data collection approaches as a routine method for room-temperature structure determination of proteins and their complexes. The growing recognition of the capabilities of SSX is leading to a few new microfocus beamlines dedicated, partly or fully, to serial crystallography. Some examples of new MX beamlines currently in operation or under construction are the I24 beamline at Diamond Light Source (Oxford, UK) (Horrell *et al.*, 2021), the ID29 beamline at the ESRF (Grenoble, France, commissioning, <https://www.esrf.fr/id29>), the MicroMAX beamline at MAX IV (Lund, Sweden, under development, <https://www.maxiv.lu.se/accelerators-beamlines/beamlines/micromax/>), TREXX at PETRA III (Hamburg, Germany, operational, [http://www.embl-hamburg.de/services/mx/P14\\_EH2/index.html](http://www.embl-hamburg.de/services/mx/P14_EH2/index.html)), BL06-XAIRA at ALBA (Barcelona, Spain, under development; Juanhuix *et al.*, 2019) and MX3 (Merlbourne, Australia, under development, <https://www.ansto.gov.au/high-performance-macromolecular-crystallography-beamline>). The successful adaptation of SSX at synchrotrons has been possible mostly due to the development of low-consumption sample delivery methods, such as the use of high-viscosity media, fixed targets and hybrid devices (see Table 1 in the review of Martin-Garcia, 2021). In addition, SSX has demonstrated a reduction in the radiation damage associated with intense beams and has opened up new opportunities for studying irreversible reactions in crystals on a wide range of time scales (Mehrabi *et al.*, 2019, 2020; Schulz *et al.*, 2018).

The MX beamline at ALBA synchrotron light source, BL13-XALOC, opened for general user operation in July 2012 (Juanhuix *et al.*, 2014). The beamline delivers a flux of  $2 \times 10^{12}$  photons  $\text{s}^{-1}$  into a variable focus of 50–300  $\mu\text{m}$  (H)  $\times$  6–100  $\mu\text{m}$  (V) at a 250 mA storage ring current, with photon energies between 4.6 and 23 keV (2.6–0.52  $\text{\AA}$ ). With its current flexible design, high brightness and mid-size beam capacity, it is focused on solving difficult crystallographic challenges. It supports a wide range of MX data collection methods, including raster optimization of diffraction from inhomogeneous crystals, high-resolution data collection from large-unit-cell crystals, room-temperature data collection on crystals that are difficult to freeze and the study of conformational dynamics, semi-automated data collection for sample-screening and ligand binding studies. We have now augmented its capabilities to include SSX experiments. BL13-XALOC is equipped with a PILATUS 6M photon-counting detector (DECTRIS, Baden, Switzerland), a fast read-out detector that can reduce the data collection time, which is important for applications such as serial crystallography. With associated sample lifetimes as short as a few milliseconds, a new rapid sample-delivery method has been implemented at BL13-XALOC, *i.e.* a high-viscosity injector, which was recently acquired from Uwe Weierstall at Arizona State University (Weierstall *et al.*, 2014).

In the work presented here, the first SSX experiments with viscous jets at BL13-XALOC have been conducted which have paved the way to obtain the first SSX membrane protein structure at the beamline (Kovalev *et al.*, 2020). The diffraction data quality from all samples tested in this study confirms that

the current capabilities of BL13-XALOC enables high-resolution determination of protein structures from microcrystals as small as 15  $\mu\text{m}$  using viscous jets. In addition, we have analyzed the site-specific radiation damage of the crystals by measuring the *B*-factor of cysteine disulfide bonds in two of the proteins analyzed, following an adapted protocol described by Weik *et al.* (2000), which shows that the approach used in this article has, overall, negligible radiation damage and a negligible effect on cysteine disulfides. Thus, BL13-XALOC can provide an interesting alternative to conventional XFELs when determining the static structures of macromolecules. The adaptation of SSX with viscous jets at BL13-XALOC will push the frontier of synchrotron crystallography by enabling its users to determine high-quality structures from difficult-to-crystallize targets like membrane proteins, using crystals of a few micrometres in size.

## 2. Materials and methods

### 2.1. Microcrystal sample preparation

Hen egg-white lysozyme and proteinase K from *Tritirachium album* were purchased from Sigma–Aldrich with reference numbers 62970 and P2308, respectively, and their crystals grown on-site in 0.1 *M* sodium acetate (pH 3.0), 18% (*w/v*) sodium chloride and 6% PEG 400 for lysozyme, and in 0.1 *M* MES (pH 6.5), 0.5 *M* sodium citrate and 0.1 *M* calcium chloride for proteinase K, using the batch method described previously (Martin-Garcia *et al.*, 2017). Phycocyanin was purified and microcrystals grown in 75 *mM* HEPES (pH 7.0), 20 *mM* magnesium chloride and 9% PEG 3350 as reported previously (Martin-Garcia *et al.*, 2017) at Arizona State University labs, and shipped to ALBA experimental laboratories in a 4°C thermo-box prior to the experiment. The SH3 domain of  $\alpha$ -spectrin ( $\alpha$ -spectrin-SH3) was purified in ALBA experimental laboratories as described previously (Sadqi *et al.*, 1999) and was subjected to a final purification step using a SEC column previously equilibrated in 10 *mM* citric acid (pH 3) and 150 *mM* sodium chloride.  $\alpha$ -Spectrin-SH3 crystals were obtained by applying several concentration/dilution steps with milli-Q water inside standard Amicon Ultra 0.5 ml centrifugal filters (3 kDa cutoff) at 4°C. A crystalline slurry appeared when most of the citric acid buffer was removed. Human insulin was purchased from Sigma–Aldrich with reference number 11376497001. Insulin powder was dissolved in 5 *mM* zinc chloride and 25 *mM* HCl at a concentration of 5–10  $\text{mg ml}^{-1}$ . Cuboid-shaped microcrystals were obtained in 35.2 *mM* sodium citrate (pH 7) and 5% (*v/v*) acetone as precipitant by the batch method using agarose gel at 0.1% as medium for growing the crystals as described previously (Artusio *et al.*, 2020). Crystal size varied between 20  $\mu\text{m} \times 10 \mu\text{m} \times 5 \mu\text{m}$  for lysozyme, 15  $\mu\text{m} \times 10 \mu\text{m} \times 5 \mu\text{m}$  for proteinase K, 20  $\mu\text{m} \times 15 \mu\text{m} \times 5 \mu\text{m}$  for phycocyanin, 30  $\mu\text{m} \times 5 \mu\text{m} \times 5 \mu\text{m}$  for  $\alpha$ -spectrin-SH3 and 30  $\mu\text{m} \times 30 \mu\text{m} \times 30 \mu\text{m}$  for insulin (Table 1). Microcrystals of all proteins tested are shown in Fig. 1. Lipidic cubic phase (LCP) was prepared using 9.9 MAG monoolein (1-oleoyl-*rac*-gly-

**Table 1**  
Data collection statistics (values in parentheses are for the high-resolution shell).

	Lysozyme	Proteinase K	Phycocyanin	$\alpha$ -Spectrin-SH3	Insulin
Beamline	BL13 XALOC	BL13 XALOC	BL13 XALOC	BL13 XALOC	BL13 XALOC
Wavelength (Å)	0.98	0.98	0.98	0.98	1.28
Temperature (K)	295	295	295	295	295
Crystal size (µm)	10 × 10 × 5	15 × 10 × 5	20 × 15 × 5	30 × 5 × 5	20 × 30 × 30
Flow rate (nl min <sup>-1</sup> )	29.4	29.4	29.4	71.4	71.4
Exposure time (ms)	80	80	80	80	80
Data collection time (h)	2.6	11	17	3	7
Sample consumption (µl)	4.5	19.4	30	14	30
Max. dose per crystal (KGy)	115	115	125	98.4	150
Crystal-detector distance (mm)	506	506	506	506	506
No. of images collected	114080	577904	753533	139971	433986
No. of indexed patterns	23733	216645	152142	13039	51144
Space group	<i>P</i> <sub>4</sub> <sub>3</sub> <sub>2</sub> <sub>1</sub> <sup>2</sup>	<i>P</i> <sub>4</sub> <sub>3</sub> <sub>2</sub> <sub>1</sub> <sup>2</sup>	<i>H</i> <sub>3</sub> <sup>2</sup>	<i>P</i> <sub>2</sub> <sub>1</sub> <sub>2</sub> <sub>1</sub>	<i>H</i> <sub>3</sub>
<i>a</i> , <i>b</i> , <i>c</i> (Å)	79.00, 79.00, 38.2	68.40, 68.40, 108.4	188.5, 188.5, 61.0	34.2, 42.6, 50.8	81.6, 81.6, 33.6
$\alpha$ , $\beta$ , $\gamma$ (°)	90, 90, 90	90, 90, 90	90, 90, 120	90, 90, 90	90, 90, 420
Resolution range (Å)	38.2–2.1 (2.17–2.1)	48.4–1.9 (1.97–1.9)	48.8–2.1 (2.17–2.1)	42.6–2.1 (2.17–2.1)	30.3–1.7 (1.76–1.7)
Total No. of reflections	5 089 514 (115 198)	78 935 391 (640 218)	72 742 152 (1 687 827)	1 145 735 (25 647)	11 811 721 (817 546)
No. of unique reflections	7498 (716)	21 010 (2033)	24 059 (2370)	4682 (454)	9140 (928)
Completeness (%)	100 (100)	100 (100)	100 (100)	100 (100)	100 (100)
Redundancy	679 (161)	3757 (315)	3023 (712)	245 (57)	1292 (881)
$\langle I/\sigma(I) \rangle$	9.8 (0.5)	17.4 (0.6)	12.6 (0.6)	6.5 (0.3)	7.9 (1.5)
CC* (%)	99.90 (58.55)	99.96 (60.67)	99.92 (29.60)	99.75 (58.17)	99.47 (73.28)
<i>R</i> <sub>split</sub>	7.6 (157.9)	4.6 (145.1)	7.7 (231.1)	10.1 (229.7)	12.3 (74.8)
Wilson <i>B</i> -factor (Å <sup>2</sup> )	37.4	23.7	42.3	50.3	29.1

cerol) purchased from Sigma–Aldrich (M7765) as described previously (<https://cherezov.usc.edu/reconstitution.htm>). For all samples tested, the crystal density was adjusted before mixing them with LCP, so that mainly single-crystal hits were observed for all samples tested. Crystal mixtures were loaded directly from a Hamilton syringe into the high-viscosity injector (Weierstall *et al.*, 2014).

**2.2. Data collection**

Diffraction data collection of serial snapshots (*i.e.* no crystal rotation during X-ray exposure) from lysozyme, proteinase K, phycocyanin,  $\alpha$ -spectrin-SH3 and insulin microcrystals was

performed on the BL13-XALOC end-station at ALBA Synchrotron in Spain (Juanhuix *et al.*, 2014). Crystals embedded in LCP were streamed across the X-ray beam using a high-viscosity injector (Weierstall *et al.*, 2014) using a fused-silica capillary with an inner diameter of 50 µm. A 20 µl sample reservoir was used in all experiments. Measurements were performed using the experimental set-up described in §3.1. The crystal carrier stream was extruded out of the nozzle by a pressure that varied between 0.1 and 2.1 MPa, depending on the flow rate of the sample, which was varied from 29.4 to 88.2 nl min<sup>-1</sup>, depending on the sample nature (buffer composition and crystal density) and the observed diffraction, corresponding to an average jet velocity of between 249.6 and

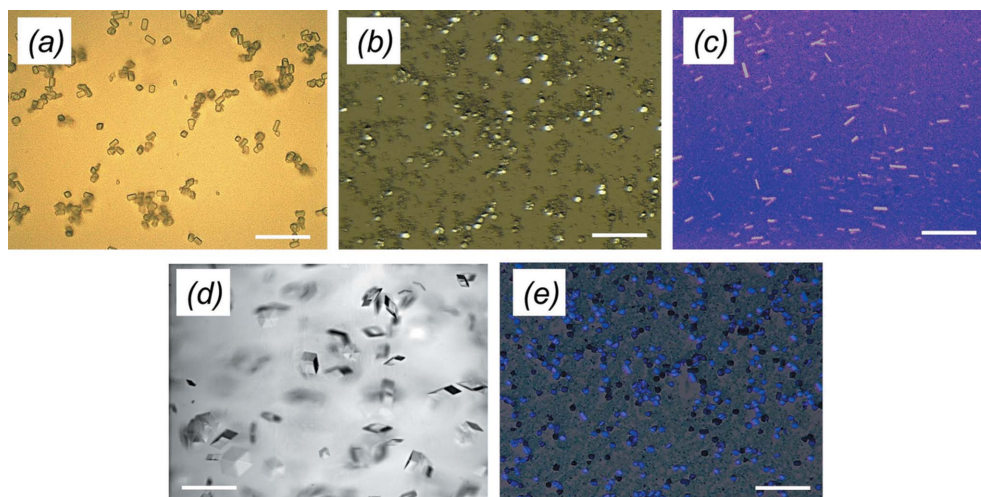


**Figure 1**  
Protein microcrystals at ALBA, showing (a) lysozyme, (b) proteinase K, (c)  $\alpha$ -spectrin-SH3, (d) insulin and (e) phycocyanin. The scale bar represents 100 µm.

749  $\mu\text{m s}^{-1}$  in the 50  $\mu\text{m}$  diameter nozzle. To prevent the viscous medium stream from curling, a helium-gas sheath was introduced at the point of extrusion. An in-line high-resolution microscope was used to align the nozzle to the beam and to observe the stream. Data were collected at an X-ray energy of 12.6 keV (0.98 Å) for all proteins except for insulin, where the data set was collected at the Zn *K*-edge of 9.7 keV (1.28 Å). All snapshots for all proteins were collected on a PILATUS 6M detector running in a continuous shutterless mode at a frame rate of 12 Hz (80 ms exposure time), while crystals passed through an X-ray beam of 50  $\mu\text{m} \times 10 \mu\text{m}$  (H  $\times$  V) in size. Since crystals had similar diffraction quality, the sample-to-detector distance was kept constant at 506 mm. Data collection statistics are shown in Table 1.

### 2.3. Data processing and structure determination

All images (in cbf format) were subjected to peak finding, indexing and merging using the software package *CrystFEL* (White, 2019; White *et al.*, 2012). For all proteins, all steps of this analysis were performed using *CrystFEL* Version 0.10.0 (<https://www.desy.de/~white/crystfel/download.html>). The peak-finder8 algorithm was used for peak finding with the following parameters: threshold = 30; min-snr = 2; int-rad = 2, 4 and 6; and indexing was performed using *XGANDALF* (Gevorkov *et al.*, 2019), *MOSFLM* (Powell *et al.*, 2013) and *DirAx* (Duisenberg, 1992), in that order.

Lysozyme and proteinase K were solved in the space group  $P4_32_12$  using a tetragonal cell ( $a = b = 79.0$ ,  $c = 38.2$  Å and  $\alpha = \beta = \gamma = 90^\circ$  for lysozyme, and  $a = b = 68.4$ ,  $c = 108.4$  Å and  $\alpha = \beta = \gamma = 90^\circ$  for proteinase K), and merged in point the group  $4/mmm$ .  $\alpha$ -Spectrin-SH3 was indexed and merged in the space group  $P2_12_12_1$  using the orthorhombic cell ( $a = 34.2$ ,  $b = 42.6$ ,  $c = 50.8$  Å and  $\alpha = \beta = \gamma = 90^\circ$ ) and merged in the point group  $mmm$  using *partialator* by applying three iterations and the ‘unity’ model (White, 2019). For all proteins, the merged *hkl* files were converted to the *mtz* format with the intermediate step of first converting to *XSCALE* format and then to *mtz* using the *XDS* program (Kabsch, 2010). The intensities were converted to structure factor amplitudes using *AIMLESS* (Evans, 2011; Evans & Murshudov, 2013) from the CCP4 program suite (Winn *et al.*, 2011). While all of the collected data were included for structure determination (see Tables S1 and S2 of the supporting information), it can be seen that  $\sim 50\,000$  indexable patterns for proteinase K and  $\sim 10\,000$  indexable patterns for lysozyme would be sufficient for reaching acceptable data-quality statistics and full completeness for the same resolution range. This would correspond to data collection times of only  $\sim 2$  and 1 h, respectively.

The lysozyme and proteinase K phases were calculated by molecular replacement with *MOLREP* (Lebedev *et al.*, 2008; Vagin & Teplyakov, 2010) using the PDB entries 1vds (unpublished work) and 1ic6 (Betzel *et al.*, 2001), respectively, as reference models, with all solvent atoms removed.  $\alpha$ -Spectrin-SH3 phases were determined with *MOLREP* using PDB entry 4f17 (unpublished work) as the search model, with all solvent atoms removed. Insulin was solved in the space group  $H3$

(unit-cell dimensions  $a = b = 81.6$ ,  $c = 33.6$  Å,  $\alpha = \beta = 90^\circ$  and  $\gamma = 120^\circ$ ) of a trigonal cell with hexagonal axes. After indexing, *ambigator* was used to resolve the indexing ambiguity due to serial data collection for this point group (applying operators  $k, h, -l; -h, h+k, -l$  and  $-h, -k, l$ ) and then merged into point group  $-3_H$ . Phycocyanin was indexed into the hexagonal unit cell  $a = b = 188.5$ ,  $c = 61.0$  Å,  $\alpha = \beta = 90^\circ$  and  $\gamma = 120^\circ$ , and the indexing ambiguity solved prior to merging into  $-3ml_H$ . Phasing was performed with *MOLREP* using the coordinates from PDB entry 5uvk (Martin-Garcia *et al.*, 2017) for phycocyanin and 4ey9 (Fávero-Retto *et al.*, 2013) for insulin as reference models. All five structures were refined using alternate cycles of restrained refinement with *REFMAC5* (Murshudov *et al.*, 2011) and manual refinement in *COOT* (Emsley *et al.*, 2010). The structures were then submitted to the PDB-REDO server (Joosten *et al.*, 2009) for final refinement before being deposited in the PDB.

The maximum radiation dose per crystal was estimated using the RADDPOSE-3D server (Zeldin *et al.*, 2013), assuming cuboid crystals for all four crystal dimensions tested in this study (see §2.2), a beam size of 50  $\mu\text{m} \times 10 \mu\text{m}$ , a photon flux of  $2 \times 10^{12}$  photons  $\text{s}^{-1}$ , an energy of 12.6 keV and an exposure time of 80 ms. These estimates varied from 98 to 150 K Gy per crystal, as summarized in Table 1. Crystal structure superposition and calculation of the root-mean-square deviation (RMSD) values were performed using the *LSQKAB* program (Kabsch, 1976). All figures were prepared with *UCSF CHIMERA*X (Version 1.2.4) (Goddard *et al.*, 2018; Pettersen *et al.*, 2004).

### 2.4. Site-specific radiation damage analysis

Site-specific radiation damage analysis was carried out on all protein structures presented in this study using the *RABDAM* program (Shelley *et al.*, 2018), recently implemented in the CCP4 program suite (Winn *et al.*, 2011). An adaptation of the available Python scripts reported by Shelley *et al.* was used to obtain the data files from the analyzed PDBs and to draw the plots showing the  $B_{\text{Damage}}$  distributions corresponding to either the whole protein, some side-chain terminal atoms or cysteine S atoms (always excluding all H atoms). We applied default values of 7 Å to calculate the packing density and a sliding window of 2%, as suggested in Shelley *et al.* (2018).

The site-specific radiation damage was further evaluated by recording the *B*-factor of the final refined models of the atoms of the cysteine residues of lysozyme and proteinase K involved in disulfide bonds. The residue pairs in question were Cys6/Cys127, Cys30/Cys115, Cys64/Cys80 and Cys76/Cys94 for lysozyme, and Cys34/Cys123 and Cys178/Cys249 for proteinase K. The ratios between the  $S_\gamma$  and  $C_\beta$  atoms were calculated for all the individual residues, and then these ratio values were averaged for the  $S_\gamma/C_\beta$  pairs for each respective disulfide bond, resulting in a single number for each cysteine pair forming a disulfide bond. For comparison, these numbers were also calculated for a series of relevant PDB structures as described in the *Results and discussion* section (§3).



### 3. Results and discussion

In this study, we demonstrate that SSX with viscous jets is feasible at BL13-XALOC and can be used to determine the structures of a range of proteins of different sizes and types from crystal sizes between 15 and 30  $\mu\text{m}$ . To deliver the microcrystals into the X-ray beam, we used a high-viscosity injector (Weierstall *et al.*, 2014). Diffraction data were collected in a continuous shutterless mode using a PILATUS 6M detector operating at 12 Hz. The experimental set-up is shown in Fig. 2. We successfully collected excellent quality full data sets for five different proteins, presented below. In addition to the standard model system, *i.e.* proteins such as hen egg-white lysozyme and proteinase K from *Tritirachium album limber*, we included phycocyanin from *Thermosynechococcus elongatus*, human insulin and the SH3 domain of  $\alpha$ -spectrin ( $\alpha$ -spectrin-SH3) from *Gallus gallus*.

#### 3.1. Experimental set-up at the BL13-XALOC end-station

Serial data collection was performed at BL13-XALOC at ALBA, a third-generation synchrotron radiation source (Barcelona, Spain). A detailed description of the beamline end-station can be found in Juanhuix *et al.* (2014). BL13-XALOC is a 30 m-long (from the photon source) energy-tunable beamline at the 3 GeV storage ring of ALBA which operates at a final current of 250 mA. It is fed by a 2 m-long in-vacuum undulator (IVU21) (Bruker Advanced Supercon, Bergisch Gladbach, Germany), with a minimum gap of 5.7 mm, and placed in a medium straight section of the storage ring. The focused X-ray beam has a cross-section of  $50 \mu\text{m} \times 10 \mu\text{m}$  full width at half-maximum (FWHM) at the sample

position, with a photon flux of  $2 \times 10^{12}$  photons  $\text{s}^{-1}$  at 250 mA ring current and an energy ranging from 4.6 to 23 keV. The beamline optics consist of an Si(111) double-crystal monochromator and a pair of focusing mirrors in Kirkpatrick–Baez geometry (Kirkpatrick & Baez, 1948).

The BL13-XALOC end-station is based on two in-house-developed positioning tables (Colldelram *et al.*, 2010) that support the detector and the diffractometer together with the beam-conditioning elements. The sample-viewing system, an OAV B-ZOOM (ARINAX), consists of an on-axis parallax-free high-resolution video microscope (0.16  $\mu\text{m}/\text{pixel}$  at maximum zoom) and a user-controlled front light and a polarized back light (transmitted). The experimental station consists of an MD2M diffractometer (Maatel), a PILATUS 6M hybrid pixel detector (DECTRIS, Switzerland), which can collect full-frame data with a frequency of up to 12.5 Hz in shutterless mode, and a CATS automatic sample exchanger (IRELEC).

To avoid collision with existing hardware, the sample injector was installed on a fixed translational stage at  $45^\circ$  to the X-ray beam. A schematic view of the experimental set-up used at BL13-XALOC is shown in Fig. 2. A standard fast protein liquid chromatography (FPLC) instrument (ÄKTA Pure 25M) was used to extrude the samples out of the injector, and helium was employed as sheath gas to keep the extruded stream stable. For the experiment, an upgraded version of the injection system used in previous experiments at synchrotrons (Martin-Garcia *et al.*, 2017, 2019; Nogly *et al.*, 2015) was installed at BL13-XALOC. The upgrades include the following modifications: (1) the output of a pressurized isopropanol reservoir can be coupled into the sheath gas line

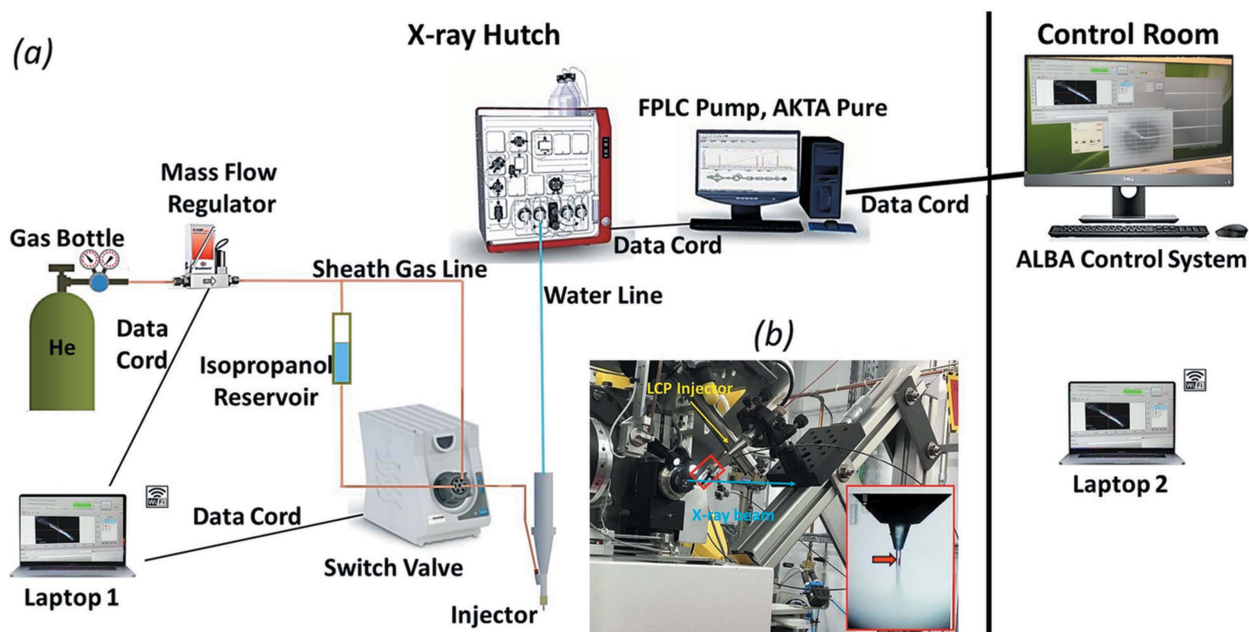


**Figure 2** Experimental  $45^\circ$  set-up at BL13-XALOC. (a) Schematic diagram of the high-viscosity injector operation system showing all equipment and parts used for the set-up. A conventional FPLC pump was used. Helium was used as sheath gas in all our experiments. (b) High-viscosity injector (Weierstall *et al.*, 2014) mounted on translation stages. The inset panel shows a closer view of the LCP stream extruding from a  $50 \mu\text{m}$  glass capillary nozzle. The red arrow indicates the position of the X-ray beam.

Table 2

Data refinement statistics (values in parentheses are for the high-resolution shell).

	Lysozyme	Proteinase K	Phycocyanin	$\alpha$ -Spectrin-SH3	Insulin
Resolution range (Å)	35.35–2.1 (2.16–2.10)	44.21–1.9 (1.95–1.9)	43.4–2.1 (2.16–2.1)	32.6–2.1 (2.16–2.1)	24.35–1.71
Completeness (%)	100 (100)	100 (100)	99.2 (90.0)	99.1 (88.1)	99.7 (96.0)
No. of reflections, working set	6723 (479)	19879 (1431)	22830 (1530)	4110 (264)	8163 (584)
No. of reflections, test set	741 (59)	1071 (79)	1185 (78)	503 (33)	908 (56)
$R_{\text{work}}$ (%)	17.9	16.5	30.5	19.4	24.0
$R_{\text{free}}$ (%)	23.2	19.6	34.7	23.9	25.8
No. of atoms					
Protein	1001	2068	2488	462	808
Ions	1	2	2	0	3
Ligands	0	4	138	0	0
Water	17	89	43	5	15
Total	1019	2163	2671	467	826
R.m.s. deviations					
Bonds (Å)	0.010	0.011	0.005	0.012	0.006
Angles (°)	1.582	1.596	1.162	1.826	1.271
Average $B$ -factors (Å <sup>2</sup> )					
Protein	46.9	30.4	53.9	62.1	33.0
Ions	64.5	33.0	92.8	0	35.1
Ligands	0	55.3	57.6	0	0
Water	40.0	35.1	47.4	59.7	34.2
Ramachandran plot					
Favoured (%)	96.1	96.0	97.6	98.2	94.7
Allowed (%)	3.9	3.6	2.1	1.8	4.3
PDB code	7s4w	7s4z	7s4z	7s4r	7s4y

through a Rheodyne valve (IDEX MXP7970-000), which enabled switching between sheath gas and isopropanol at the nozzle when needed; (2) a remote-control system for the Rheodyne valve and gas flow controller comprised of two laptops (one in the X-ray hutch and another in the control room), connected wirelessly. This enabled us to remotely control the gas flow and wash the aperture of the nozzle with isopropanol (to remove viscous medium build-up) from outside the X-ray hutch if the sample stream was not stable or if it clogged. In addition, the new injector reservoirs are made of titanium, which is more durable and resistant to corrosion.

### 3.2. Structural data analysis

**3.2.1. Model proteins lysozyme and proteinase K.** Both lysozyme and proteinase K were crystallized, pelleted and then suspended in LCP as described previously (Martin-Garcia *et al.*, 2017). The corresponding microcrystal–LCP suspension containing lysozyme or proteinase K microcrystals were then loaded into the high-viscosity injector (Weierstall *et al.*, 2014) and diffraction data were collected using a flow rate of 29.4 nl min<sup>-1</sup> for both samples. Lysozyme and proteinase K crystals belonged to the space group  $P4_32_12$ , and data were recorded up to maximum resolutions of 2.1 and 1.9 Å, respectively. For lysozyme, a total of 114080 images were recorded in an effective measuring time of 2 h 34 min, 23733 of which were successfully indexed (combined hit and indexing rate = 21%) and merged. A diffraction pattern from a lysozyme microcrystal is shown in Fig. S1 (see supporting information). The structure of lysozyme was solved by molecular replacement using the previously solved structure (PDB entry 1vds, to be published) as a reference model with all solvent molecules removed. The final structure was refined to

2.1 Å resolution with  $R_{\text{work}}$  and  $R_{\text{free}}$  values of 17.9 and 23.2%, respectively (Table 2). As for proteinase K, 577904 images were recorded in 13 h 46 min, which resulted in a sample consumption of 19.4 µl. This resulted in a total of 216645 successfully indexed (combined hit and indexing rate = 32%) and merged patterns. Despite carefully mixing of the microcrystals with LCP to reach a homogenous sample, multi-crystal diffraction was observed (Fig. S2 in the supporting information). The *CrystFEL* internal architecture (Version 0.5.0; <https://www.desy.de/~twhite/crystfel/relnotes-0.5.0>) was changed so that it can index multiple crystal lattices in one image. The structure of proteinase K was solved by molecular replacement using the previously solved cryogenic structure (PDB entry 1ic6; Betzel *et al.*, 2001) as a reference model with all solvent molecules removed. The final structure was refined to 1.9 Å resolution with  $R_{\text{work}}$  and  $R_{\text{free}}$  values of 16.5 and 19.6%, respectively (Table 2). The final data collection and refinement statistics of lysozyme and proteinase K are given in Tables 1 and 2.

The high quality of the lysozyme and proteinase K structures can be assessed from the electron density maps 2mF<sub>o</sub>-DF<sub>c</sub> for the active site residues of lysozyme, and the two calcium ions, and neighbouring residues of proteinase K (Fig. 3). Further evaluation of the quality of the structures was carried out by comparing them with previously reported crystal structures determined at room temperature using SSX, such as PDB entries 4rlm (Botha *et al.*, 2015), 4z98 (Murray *et al.*, 2015) and 4x3b (Roedig *et al.*, 2015) for lysozyme, and 5uvl (Martin-Garcia *et al.*, 2017), 6fjs (Botha *et al.*, 2018) and 5mj1 (Meents *et al.*, 2017) for proteinase K. Overall, all the lysozyme and proteinase K structures aligned very well with each other, with average RMSD values of 0.215 and 0.172 Å for the C<sup>α</sup> atoms of lysozyme and proteinase K, respectively. The

average RMSD values for all atoms (0.681 and 0.447 Å for the C $\alpha$  atoms of lysozyme and proteinase K, respectively) indicate slightly higher differences, which are mainly found in the loop regions, as well as in the solvent-exposed regions, as one would expect.

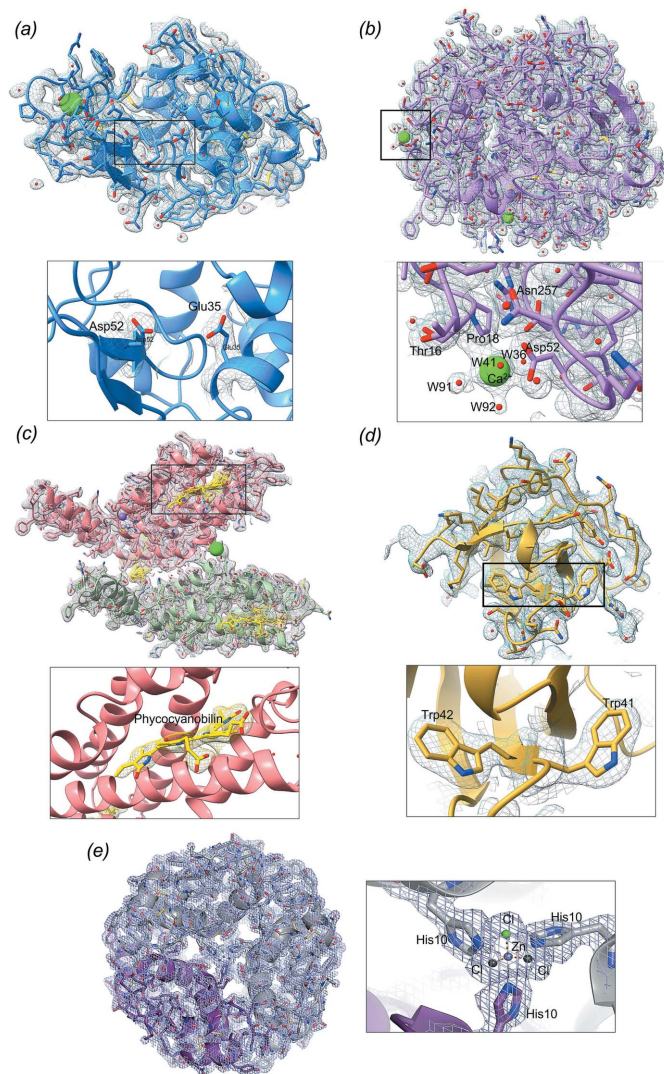


**Figure 3**

Quality of the 2mFo-DFc electron density maps for all structures tested contoured at  $1\sigma$ . (a) Lysozyme illustrated as a blue cartoon and stick representation. Solvent molecules (water in red) and Cl $^{-}$  ions (green) are represented as spheres. A closer view (panel below) of the Glu35 and Asp52 residues at the catalytic site. (b) Proteinase K illustrated as a pink cartoon and stick representation. Solvent molecules (water in red) and the Ca $^{2+}$  ion (green) are represented as spheres. A closer view (panel below) of one of the Ca $^{2+}$  ions. (c) The two phycocyanin subunits ( $\alpha$  green and  $\beta$  salmon) illustrated as a blue cartoon and stick representation. The chromophores are shown in a yellow cartoon and stick representation. Solvent molecules (water in red), Na $^{+}$  ions (purple) and Cl $^{-}$  ions (green) are represented as spheres. A closer view (panel below) of the phycocyanobilin chromophore. (d) The  $\alpha$ -spectrin-SH3 domain illustrated as a yellow cartoon and stick representation. Water molecules are shown as red spheres. A closer view (panel below) of the Trp41 and Trp42 residues at the binding site. (e) Hexameric human insulin illustrated as a purple cartoon and stick representation. The dimer in the asymmetric unit is shown in purple and symmetry-related molecules are shown in dark grey. A closer view (right panel) of the coordination of the Zn $^{2+}$  ion (blue) with the His10 residues (sticks), and the Cl $^{-}$  ions (in green, and black for the symmetry-related molecules).

**3.2.2. Phycocyanin.** Microcrystals of phycocyanin, a photosynthetic pigment from the thermophilic cyanobacterium *T. elongatus*, were suspended in LCP and extruded at a flow rate of 29.4 nl min $^{-1}$ . A total of 753 533 images were collected from 30  $\mu$ l of sample in about 23 h (Table 1), from which 152 142 patterns were successfully indexed (combined hit and indexing rate = 20%) and merged. A representative diffraction pattern from the phycocyanin sample is shown in Fig. S3 (see supporting information). The structure of phycocyanin was determined by molecular replacement using the previously solved PDB crystal structure 5uvk (Martin-Garcia *et al.*, 2017) as the search model and refined to a 2.1 Å resolution with final  $R_{\text{work}}$  and  $R_{\text{free}}$  values of 30.5 and 34.7%, respectively (Table 2). The final data collection and refinement statistics are shown in Tables 1 and 2. The quality of our structural model can be assessed from the 2mFo-DFc electron density maps for one of the chromophores of the protein, shown in Fig. 3.

Further assessment of the quality of the obtained structure was carried out by superimposing it with room-temperature structures: the two SSX structures recently described using viscous jets, PDB entries 5uvk (Martin-Garcia *et al.*, 2017) and 5mjg (Meents *et al.*, 2017), and the two SFX structures determined by Fromme and co-workers, PDB entries 4ziz (Fromme *et al.*, 2015) and 4q70 (to be published). As indicated by the RMSD values for the C $\alpha$  atoms (0.366 Å) and all atoms (0.480 Å), overall, our structure superimposed very well with all phycocyanin structures, with slight differences observed in the solvent-exposed regions.

**3.2.3.  $\alpha$ -Spectrin-SH3.** The  $\alpha$ -spectrin-SH3 domain is a small module of about 60 residues found in the  $\alpha$ -spectrin protein that mediate transient protein–protein interactions relative to many cellular processes by recognizing polyproline-rich motifs in its protein targets (Kurochkina & Guha, 2013). Microcrystals of the  $\alpha$ -spectrin-SH3 domain were suspended in LCP and delivered to the X-ray beam at a flow rate of 71.4 nl min $^{-1}$  for about 3 h 39 min to collect a total of 139 971 images from nearly 14  $\mu$ l of sample. From all patterns collected, 13 039 patterns were successfully indexed (combined hit and indexing rate = 9%) and merged. A diffraction pattern representative of the  $\alpha$ -spectrin-SH3 microcrystals sample is shown in Fig. S4 (see supporting information). The structure of the  $\alpha$ -spectrin-SH3 domain was determined by molecular replacement using the synchrotron structure at 100 K reported by Cámara-Artigas *et al.* (PDB entry 4f17, to be published), and refined to a 2.1 Å resolution with final  $R_{\text{work}}$  and  $R_{\text{free}}$  values of 19.4 and 23.94%, respectively. The data collection and refinement statistics are summarized in Tables 1 and 2.

The quality of the  $\alpha$ -spectrin-SH3 structure was further evaluated by comparing it with two previously reported cryo-cooled structures, namely, PDB entries 4f16 (Cámara-Artigas and Gavira, unpublished results) and 2nuz (Agarwal and co-workers, unpublished results). Based on the RMSD values for the C $\alpha$  atoms (0.265 Å) and all atoms (0.762 Å), our structure aligned very well with the three  $\alpha$ -spectrin-SH3 structures, with major coordinate differences observed in the loops



regions, as reported in previous structures (Cámara-Artigas *et al.*, 2011).

**3.2.4. Insulin.** Cuboid-shaped microcrystals of insulin grown in agarose gel at 0.1% (Artusio *et al.*, 2020) were suspended in LCP and extruded at a flow rate of 71.4 nl min<sup>-1</sup> for 10 h 28 min to collect a total of 433 986 images, with an effective consumption of 30 µl of sample suspension. A total of 51 144 patterns were successfully indexed (combined hit and indexing rate = 12%) and merged. A diffraction pattern representative of a single insulin microcrystal is shown in Fig. S5 (see supporting information). All data collection statistics are shown in Table 1. The structure of insulin was determined by molecular replacement using the crystal structure for PDB entry 4ey9 (Fávero-Retto *et al.*, 2013) as the search model. The structure, containing two protein monomers and three ions (2 × Zn<sup>2+</sup> plus 1 × Cl<sup>-</sup>) in the asymmetric unit forming the typical T6 hexameric assembly of human insulin, was refined to 1.7 Å, with final  $R_{\text{work}}$  and  $R_{\text{free}}$  values of 24.0 and 25.8%, respectively (Table 2). The quality of our structural model can be assessed from the 2mFo-DFc electron density maps for one of the two Zn<sup>2+</sup> ions (Fig. 3).

To evaluate the quality of our structure model, we superimposed it with previously reported cryogenic human insulin structures, PDB entries 1os3 (Smith & Blessing, 2003), 4f0n (Fávero-Retto *et al.*, 2013) and 5co2 (unpublished results). The average RMSD values for the C<sup>α</sup> atoms (0.416 Å) and all atoms (0.636 Å) show that, overall, our insulin model superimposed very well with all three insulin structures, with slight differences observed in the solvent-exposed regions, as expected.

### 3.3. Site-specific radiation damage

Site-specific radiation damage affects primarily the C–S bonds in cysteine and methionine residues, disulfide bonds and the carboxylate groups of negatively charged residues of Asp and Glu (Weik *et al.*, 2000). To assess the site-specific radiation damage, two independent approaches were followed, *i.e.*  $B_{\text{Damage}}$  ratio analysis (Gerstel *et al.*, 2015) and disulfide bond analysis.

**3.3.1.  $B_{\text{Damage}}$  ratio analysis.**  $B_{\text{Damage}}$  is a metric that identifies potential sites of specific damage of atoms with  $B$ -factor values relative to neighbouring atoms that occupy a similar packing density environment in the crystalline structure (Gerstel *et al.*, 2015). In this work, we used the procedure described by Gerstel *et al.* (2015) to calculate the  $B_{\text{Damage}}$  distributions of all protein atoms (*all*), the carboxylate atoms of Glu and Asp residues (*term*), and the S atoms of Cys residues (*S<sub>cys</sub>*), to verify if the structures of this study could be prone to radiation damage (Fig. 4). In order to cross-check the validity of the procedure followed here, a set of protein structures (Nanao *et al.*, 2005; Sutton *et al.*, 2013) were used for reference (Fig. S6 in the supporting information). The  $B_{\text{Damage}}$  distribution profiles of *all*, *term*, and *S<sub>cys</sub>* atoms for the five proteins collected in this work [Figs. 4(a), 4(b) and 4(c), respectively] are narrower than those from the reference data sets and have higher peaks, which results in smaller variances

(Table S3), a reduced data spread and median values closer to 1.0. According to Gerstel and co-workers, these observations are compatible with nonexistent radiation damage, with the sole exception for insulin. This protein presents a high and narrow  $B_{\text{Damage}}$  profile ( $\nu = 0.006$ ) for the *S<sub>cys</sub>* atoms [Fig. 4(c)], in which only two S atoms (corresponding to a single and most labile disulfide bond) bear higher  $B_{\text{Damage}}$  values (noticeable as a second subpeak shifted towards higher  $B_{\text{Damage}}$  values) indicative of incipient damage effects, which could be attributed to the fact that insulin data were collected at a lower energy (9.7 keV) instead of 12.6 keV as for the others. At this lower energy, more X-ray dose is deposited into the crystals (Holton, 2009; Murray *et al.*, 2004), thus increasing the probability of radiation damage. In this regard, the endogenous presence of the Zn<sup>2+</sup> ion in the insulin molecule leads to an increased absorbed dose (Garman & Owen, 2006), specially at its absorption peak, making it highly sensitive to radiation damage. In the case of phycocyanin, the *S<sub>cys</sub>* distribution broadening ( $\nu = 0.014$ ) could be attributed to the relatively high refinement statistics (Table 1), which may have contributed to cumulative errors in the  $B_{\text{Damage}}$  calculation, as RABDAM is highly sensitive to measured  $B$ -factors (Gerstel *et al.*, 2015). As for lysozyme, the  $B_{\text{Damage}}$  distribution of the structure of this work was compared with that of other lysozyme structures collected at room temperature at synchrotron sources both using SSX and the oscillation method, as well as with lysozyme structures collected at XFELs (Fig. 4). Our structure presents the second lowest  $B_{\text{Damage}}$  profile variances (Table S3 in the supporting information) for the *all* ( $\nu = 0.021$ ), *term* ( $\nu = 0.009$ ) and *S<sub>cys</sub>* ( $\nu = 0.006$ ) atoms, with high peaks closer to  $B_{\text{Damage}}$  values of 1.0, and a small data spread. A similar behaviour, but with the lowest variances, was observed for the comparison of our proteinase K structure with other proteinase K structures determined by the SSX approach (Fig. 4). In summary, neither the lysozyme nor the proteinase K structure from this work are likely to present significant symptoms of radiation damage, confirming that the SSX structures collected at BL13-XALOC are generally unaffected by X-ray dose.

**3.3.2. Disulfide bond preferential specific damage.** As mentioned above, the specific damage at disulfide bonds has been used to qualitatively evaluate the extent of site-specific radiation damage during diffraction experiments through the inspection of difference maps and by integrating different densities in the maps derived from a series of data sets with increments in the incident X-ray dose (de la Mora *et al.*, 2020; Weik *et al.*, 2000). However, when the differences in the dose are small and the data are measured using distinct X-ray sources with widely different flux, beam size and divergence, comparisons of densities are difficult to apply. Thus, we probed whether the breakage of a cysteine bond can be followed by comparing the  $B$ -factor of the  $S_{\gamma}$  atom with the  $C_{\beta}$  atoms. Fig. S7(d) (see supporting information) shows the ratio of the  $B$ -factor of the  $S_{\gamma}$  atom with respect to the  $C_{\beta}$  atom in the cysteines involved in the disulfide bonds of the acetylcholinesterase in the PDB structures collected at different doses as reported previously (Weik *et al.*, 2000), as refined by



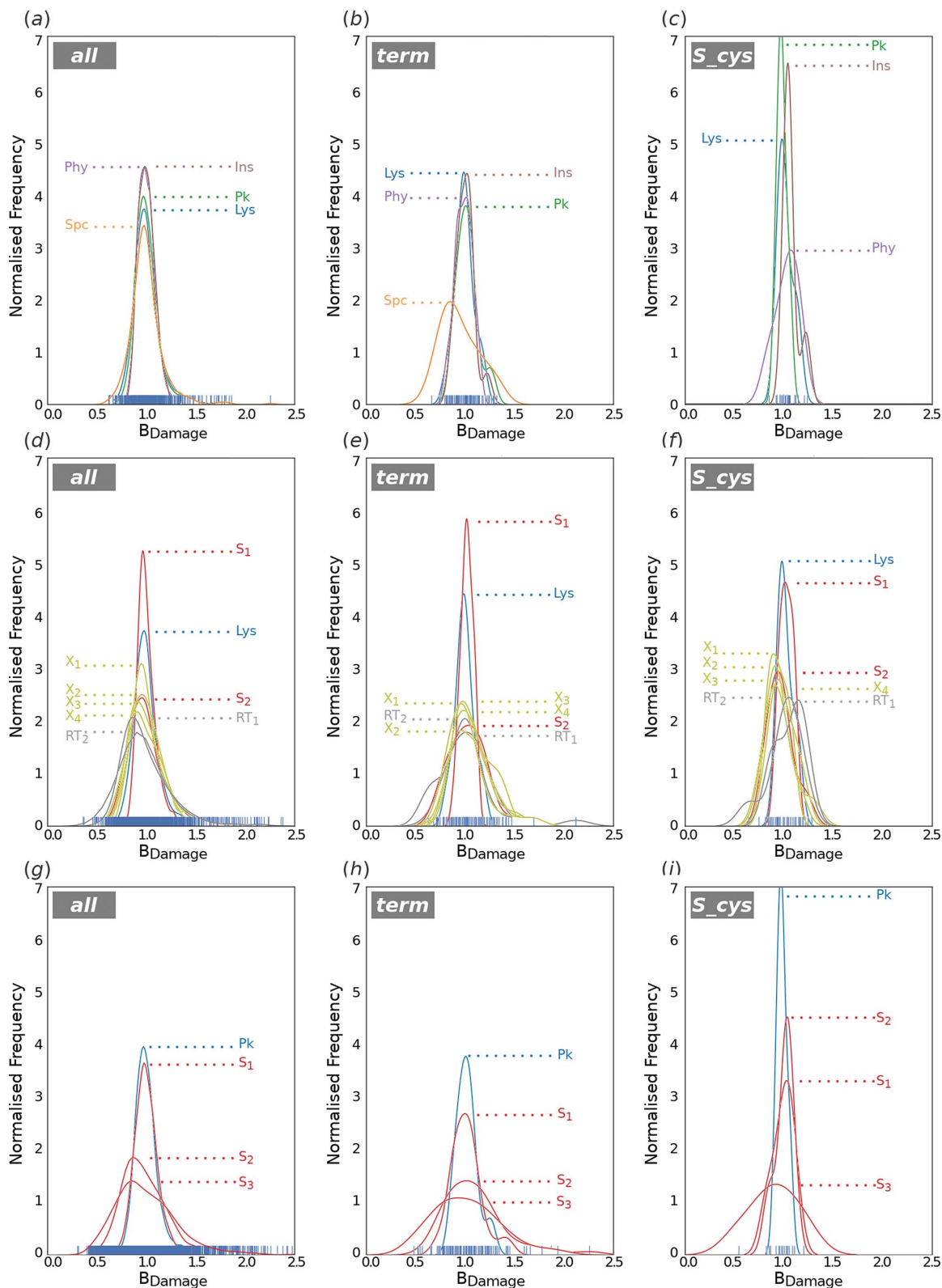


**Figure 4**

$B_{\text{Damage}}$  analysis. Distribution of protein structures of those obtained in the present work (top) and of two comparisons of the lysozyme (middle) and proteinase K (bottom) structures with other reference structures considering all protein atoms [*all*; parts (a), (d) and (g)], the terminal GLU O $\epsilon$ , ASP O $\delta$  and CYS S $\gamma$  atoms [*term*; parts (b), (e) and (h)] or only CYS S $\gamma$  atoms [*S\_cys*; parts (c), (f) and (i)]. In the top panels [parts (a), (b) and (c)], lysozyme (Lys) is depicted in blue, phycocyanin (Phy) in purple, proteinase K (Pk) in green, spectrin C (Spc) in orange and insulin (Ins) in brown. The lysozyme (middle) and proteinase K (bottom) structures of this article are shown in blue and the reference structures are shown in red; other SSX structures (Martin-Garcia, 2021) collected with a high-viscosity injector at other synchrotron beamlines (middle: S<sub>1</sub> 4rlm and S<sub>2</sub> 5uvj; bottom: S<sub>1</sub> 5uvl, S<sub>2</sub> 6fjs and S<sub>3</sub> 6mh6) are shown in red and XFEL structures (middle: X<sub>1</sub> 5dm9, X<sub>2</sub> 6h0k, X<sub>3</sub> 7byo and X<sub>4</sub> 6h0l) are shown in yellow, while synchrotron structures collected at room temperature in oscillation mode are shown in grey (middle: RT<sub>1</sub> 1iee and RT<sub>2</sub> 6qqe).

the PDB-REDO database (Joosten *et al.*, 2009), which reconstructed the  $S_\gamma$  atom initially left out of the refinement for the purpose of the difference density analysis. This analysis shows that radiation damage is strongly correlated with the dose at low doses, whereas at high doses, the complete breakage of the bond leads to a plateau [Fig. S7(d)]. This plateau is likely related to the restraints used during refinement, which couples the  $B$ -factors of adjacent atoms such that these do not diverge excessively. In addition, we compared the dose and relative  $B$ -factors of the acetylcholine (ACh) structures with other relevant PDB structures analyzed herein and find again a good correlation of the relative  $B$ -factor with dose [Fig. S7(d)]. The exception was the structure of PDB entry 6qqe (Gotthard *et al.*, 2019), which was collected with low dose at room temperature using a standard single-sweep data collection protocol. The relatively high  $B$ -factor can be explained by the fact that it took 10 s to collect the associated data set on a single crystal, during which the breakage of the disulfide bond was allowed to develop. In contrast, the data described in our study were collected from individual microcrystals in which each crystal was illuminated with X-rays for just 100 ms, thus avoiding the propagation of radiation damage in the crystals.

Figs. S7(a)–7(c) (see supporting information) show the ratio of temperature  $B$ -factor values for the  $S_\gamma/C_\beta$  atoms of cysteines involved in the disulfide bonds calculated as described in the *Materials and methods* section (§2) for the lysozyme, proteinase K and insulin structures presented herein, and for several structures deposited in the PDB, *i.e.* 6qqe (Gotthard *et al.*, 2019), 1qio (Weik *et al.*, 2000), 1iee (Sauter *et al.*, 2001) and 6ftr (Wiedorn *et al.*, 2018) for lysozyme, 2pwa (unpublished results), 5kxu (Masuda *et al.*, 2017) and 1ic6 (Betzl *et al.*, 2001) for proteinase K, and 4f1g (Fávero-Retto *et al.*, 2013) and 5e7w (Lisgarten *et al.*, 2017) for insulin. These PDBs were selected based on the relevance of the experimental conditions at which the crystal structures were collected, such as the temperature of data collection, the sample delivery method used and the X-ray radiation source.

The relative  $B$ -factors of the structures described herein show significantly lower values compared to the analyzed published structures, suggesting that radiation damage is reduced. For example, data collected at extremely brilliant XFELs using a jet stream (PDB entry 5kxu; Masuda *et al.*, 2017) showed a significant increase in the  $B$ -factors of the S atoms, indicating that site-specific radiation damage occurs. Thus, we conclude that SSX with viscous jets at synchrotrons, and in particular at BL13-XALOC, can provide data with minimal radiation damage.

#### 4. Conclusions and future directions

The advantages that microcrystals offer over their larger counterparts has triggered the desire to perform SSX at synchrotrons, resulting in a high demand from the user community. This is leading to the accelerated development of beamlines dedicated to this approach worldwide. To advance the MX capabilities at ALBA, the MX beamline BL13-

XALOC has established and included the SSX approach with viscous jets as a new method in its data collection pipeline, which can be tailored to the daily crystallographic and structural biology problems our users bring to the beamline. We have established the feasibility of performing SSX experiments at BL13-XALOC by determining high-resolution protein structures, demonstrating that the flux and the size of the focus resulted in adequate data quality. SSX with viscous jets offers a variety of advantages over standard crystallography such as: (1) solving structures in those cases where obtaining large crystals is an issue; (2) collecting room-temperature measurements, which allow us to detect and visualize functionally relevant molecular changes; (3) gaining access to ligand-binding pockets, which facilitates binding studies and fragment-based drug discovery; (4) providing electronic and spatial features to aid in the modelling of new drug-like compounds; (5) performing derivatization experiments without the need of fishing crystals; and (6) mitigating radiation damage. Based on this, it should now be feasible to conduct time-resolved pump-probe measurements to study light-induced reactions on millisecond timescales from microcrystals using the existing infrastructure at BL13-XALOC.

The upcoming ALBA II upgrade will bring this light source from a third-generation to a fourth-generation synchrotron, producing a much brighter and more coherent photon X-ray beam. The implementation of the SSX strategy will improve with the future upgrades at ALBA II, which will create a smaller brighter micro-focused beam with an intensity that is expected to increase by several orders of magnitude. These improvements, along with new developments in beamline optics and the acquisition of a faster frame-readout detector, will allow BL13-XALOC to determine macromolecular crystal structures from smaller crystals. Also, we anticipate that the increase in signal-to-noise ratio will allow a decrease of the repetition rate into the low microsecond range after the upcoming upgrade.

The structural biology program at ALBA comprises the development of a microfocus MX beamline called BL-06-XAIRA, currently in the construction phase (<https://www.cells.es/en/beamlines/bl06-xaira>). XAIRA will be dedicated to oscillation-based experiments and fixed-target serial crystallography, and will complement the scientific case of the BL13-XALOC beamline. The combination of a beam size down to  $1\ \mu\text{m} \times 1\ \mu\text{m}$ , together with the fixed target and jet approaches, will open the possibility to perform time-resolved studies with microsecond resolution ensuring that BL06-XAIRA will help to expand the toolbox of the Spanish SSX user community. The construction of BL06-XAIRA has started recently and the first users will be hosted during 2023.

Radiation damage has been a limiting factor in obtaining high-quality protein structures in standard X-ray crystallography at synchrotron sources. However, nowadays, radiation damage can be substantially mitigated by the adaptation of the SSX approach, in which the crystal structures of macromolecules are solved from data sets collected from thousands of crystals. After SSX came into play, over 40

experiments have been conducted (Martin-Garcia, 2021) and, to the best of our knowledge, site-specific radiation damage has only been reported for the disulfide bridges of lysozyme from a data set in which a much higher dose than the theoretical safe dose limit of 0.3 MGy (Nave & Garman, 2005) was reached (Coquelle *et al.*, 2015). In the study presented here, the radiation dose estimated by RADDOS 3D never went above the previously reported dose limit, which indicated that site-specific radiation damage was not significant for all protein structures but insulin, and, therefore, the integrity of the structures was not affected. This was also supported by the  $B_{\text{Damage}}$  values presented in Fig. 4. It is largely known that proteins containing redox cofactors or heavy elements in their structure are particularly more sensitive to radiation damage due to the increased probability of interaction with the X-rays. Thus, it has been reported that heavy atoms and the atoms in their proximity are areas of increased localized structural and electronic damage compared to the rest of the atoms in a protein structure (Hau-Riege *et al.*, 2004; Jurek & Faigel, 2009). In conclusion, offering SSX approaches at MX synchrotron beamlines is an important addition, offering users the option of collecting very low dose data sets even for microcrystals.

### Acknowledgements

All experiments presented in this study were carried out at BL13-XALOC at ALBA synchrotron, managed by the Consortium for the Construction, Equipment and Exploitation of the Synchrotron Light Source (CELLS). We would like to thank the entire BL13-XALOC staff and the floor coordinators for all their assistance in using the beamline. The authors of this manuscript would also like to acknowledge Ana Cámara-Artigas (University of Almería, Spain) for providing us with the clone of the SH3 domain of  $\alpha$ -spectrin.

### Funding information

The following funding is acknowledged: Ayuda de Atracción y Retención de Talento Investigador" from the Community of Madrid (scholarship No. 2019-T1/BMD-15552); STC Program of the National Science Foundation through BioXFEL (award No. 1231306); the Centre for Applied Structural Discovery (CASD) at the Biodesign Institute at Arizona State University; the Spanish Ministry of Science and Innovation, grants EQC2021-007532-P, PID2020-117028GB-I00, BIO2016-77883-C2-2-P.

### References

Artusio, F., Castellví, A., Sacristán, A., Pisano, R. & Gavira, J. A. (2020). *Cryst. Growth Des.* **20**, 5564–5571.  
 Betzel, C., Gourinath, S., Kumar, P., Kaur, P., Perbandt, M., Eschenburg, S. & Singh, T. P. (2001). *Biochemistry*, **40**, 3080–3088.  
 Botha, S., Baitan, D., Jungnickel, K. E. J., Oberthür, D., Schmidt, C., Stern, S., Wiedorn, M. O., Perbandt, M., Chapman, H. N. & Betzel, C. (2018). *IUCrJ*, **5**, 524–530.  
 Botha, S., Nass, K., Barends, T. R. M., Kabsch, W., Latz, B., Dworkowski, F., Foucar, L., Panepucci, E., Wang, M., Shoeman,

R. L., Schlichting, I. & Doak, R. B. (2015). *Acta Cryst.* **D71**, 387–397.  
 Cámara-Artigas, A., Gavira, J. A., Casares, S., García-Ruiz, J. M., Conejero-Lara, F., Allen, J. P. & Martínez, J. C. (2011). *Acta Cryst.* **D67**, 189–196.  
 Colldelram, C., Ruget, C. & Nikitina, L. (2010). *DLS Proc.* **1**, e44.  
 Coquelle, N., Brewster, A. S., Kapp, U., Shilova, A., Weinhausen, B., Burghammer, M. & Colletier, J.-P. (2015). *Acta Cryst.* **D71**, 1184–1196.  
 Duisenberg, A. J. M. (1992). *J. Appl. Cryst.* **25**, 92–96.  
 Emsley, P., Lohkamp, B., Scott, W. G. & Cowtan, K. (2010). *Acta Cryst.* **D66**, 486–501.  
 Evans, P. R. (2011). *Acta Cryst.* **D67**, 282–292.  
 Evans, P. R. & Murshudov, G. N. (2013). *Acta Cryst.* **D69**, 1204–1214.  
 Fávero-Netto, M. P., Palmieri, L. C., Souza, T. A. C. B., Almeida, F. C. L. & Lima, L. M. T. R. (2013). *Eur. J. Pharm. Biopharm.* **85**, 1112–1121.  
 Fromme, R., Ishchenko, A., Metz, M., Chowdhury, S. R., Basu, S., Boutet, S., Fromme, P., White, T. A., Barty, A., Spence, J. C. H., Weierstall, U., Liu, W. & Cherezov, V. (2015). *IUCrJ*, **2**, 545–551.  
 Garman, E. F. & Owen, R. L. (2006). *Acta Cryst.* **D62**, 32–47.  
 Gerstel, M., Deane, C. M. & Garman, E. F. (2015). *J. Synchrotron Rad.* **22**, 201–212.  
 Gevorkov, Y., Yefanov, O., Barty, A., White, T. A., Mariani, V., Brehm, W., Tolstikova, A., Grigat, R.-R. & Chapman, H. N. (2019). *Acta Cryst.* **A75**, 694–704.  
 Goddard, T. D., Huang, C. C., Meng, E. C., Pettersen, E. F., Couch, G. S., Morris, J. H. & Ferrin, T. E. (2018). *Protein Sci.* **27**, 14–25.  
 Gotthard, G., Aumonier, S., De Sanctis, D., Leonard, G., von Stetten, D. & Royant, A. (2019). *IUCrJ*, **6**, 665–680.  
 Hau-Riege, S. P., London, R. A. & Szoke, A. (2004). *Phys. Rev. E*, **69**, 051906.  
 Holton, J. M. (2009). *J. Synchrotron Rad.* **16**, 133–142.  
 Horrell, S., Axford, D., Devenish, N. E., Ebrahim, A., Hough, M. A., Sherrell, D. A., Storm, S. L. S., Tews, I., Worrall, J. A. R. & Owen, R. L. (2021). *J. Vis. Exp.* **168**, e62200.  
 Joosten, R. P., Salzemann, J., Bloch, V., Stockinger, H., Berglund, A.-C., Blanchet, C., Bongcam-Rudloff, E., Combet, C., Da Costa, A. L., Deleage, G., Diarena, M., Fabbretti, R., Fettahi, G., Flegel, V., Gisel, A., Kasam, V., Kervinen, T., Korpelainen, E., Mattila, K., Pagni, M., Reichstadt, M., Breton, V., Tickle, I. J. & Vriend, G. (2009). *J. Appl. Cryst.* **42**, 376–384.  
 Juanhuix, J., González, N., Garriga, D., Campmany, J., Marcos, J., Nikitina, L., Colldelram, C. & Nicolas, J. (2019). *AIP Conf. Proc.* **2054**, 060032.  
 Juanhuix, J., Gil-Ortiz, F., Cuní, G., Colldelram, C., Nicolás, J., Lidón, J., Boter, E., Ruget, C., Ferrer, S. & Benach, J. (2014). *J. Synchrotron Rad.* **21**, 679–689.  
 Jurek, Z. & Faigel, G. (2009). *Europhys. Lett.* **86**, 68003.  
 Kabsch, W. (1976). *Acta Cryst.* **A32**, 922–923.  
 Kabsch, W. (2010). *Acta Cryst.* **D66**, 125–132.  
 Kirkpatrick, P. & Baez, A. V. (1948). *J. Opt. Soc. Am.* **38**, 766–774.  
 Kovalev, K., Astashkin, R., Gushchin, I., Orekhov, P., Volkov, D., Zinovev, E., Marin, E., Rulev, M., Alekseev, A., Royant, A., Carpentier, P., Vaganova, S., Zabelskii, D., Baeken, C., Sergeev, I., Balandin, T., Bourenkov, G., Carpena, X., Boer, R., Maliar, N., Borshchevskiy, V., Büldt, G., Bamberg, E. & Gordeliy, V. (2020). *Nat Commun.* **11**, 2137.  
 Kurochkina, N. & Guha, U. (2013). *Biophys. Rev.* **5**, 29–39.  
 Lebedev, A. A., Vagin, A. A. & Murshudov, G. N. (2008). *Acta Cryst.* **D64**, 33–39.  
 Lisgarten, D. R., Palmer, R. A., Loble, C. M. C., Naylor, C. E., Chowdhry, B. Z., Al-Kurdi, Z. I., Badwan, A. A., Howlin, B. J., Gibbons, N. C. J., Saldanha, J. W., Lisgarten, J. N. & Basak, A. K. (2017). *Chem. Cent. J.* **11**, 73.  
 Martin-Garcia, J. M. (2021). *Crystals*, **11**, 521.  
 Martin-Garcia, J. M., Conrad, C. E., Nelson, G., Stander, N., Zatssepina, N. A., Zook, J., Zhu, L., Geiger, J., Chun, E., Kissick, D., Hilgart, M.



- C., Ogata, C., Ishchenko, A., Nagarathnam, N., Roy-Chowdhury, S., Coe, J., Subramanian, G., Schaffer, A., James, D., Ketwala, G., Venugopalan, N., Xu, S., Corcoran, S., Ferguson, D., Weierstall, U., Spence, J. C. H., Cherezov, V., Fromme, P., Fischetti, R. F. & Liu, W. (2017). *IUCrJ*, **4**, 439–454.
- Martin-Garcia, J. M., Zhu, L., Mendez, D., Lee, M.-Y., Chun, E., Li, C., Hu, H., Subramanian, G., Kissick, D., Ogata, C., Henning, R., Ishchenko, A., Dobson, Z., Zhang, S., Weierstall, U., Spence, J. C. H., Fromme, P., Zatsepin, N. A., Fischetti, R. F., Cherezov, V. & Liu, W. (2019). *IUCrJ*, **6**, 412–425.
- Masuda, T., Suzuki, M., Inoue, S., Song, C., Nakane, T., Nango, E., Tanaka, R., Tono, K., Joti, Y., Kameshima, T., Hatsui, T., Yabashi, M., Mikami, B., Nureki, O., Numata, K., Iwata, S. & Sugahara, M. (2017). *Sci. Rep.* **7**, 45604.
- Meents, A., Wiedorn, M. O., Srajer, V., Henning, R., Sarrou, I., Bergtholdt, J., Barthelmeß, M., Reinke, P. Y. A., Dierksmeyer, D., Tolstikova, A., Schaible, S., Messerschmidt, M., Ogata, C. M., Kissick, D. J., Taft, M. H., Manstein, D. J., Lieske, J., Oberthuer, D., Fischetti, R. F. & Chapman, H. N. (2017). *Nat. Commun.* **8**, 1281.
- Mehrabi, P., Müller-Werkmeister, H. M., Leimkohl, J.-P., Schikora, H., Ninkovic, J., Krivokuca, S., Andriček, L., Epp, S. W., Sherrell, D., Owen, R. L., Pearson, A. R., Tellkamp, F., Schulz, E. C. & Miller, R. J. D. (2020). *J. Synchrotron Rad.* **27**, 360–370.
- Mehrabi, P., Schulz, E. C., Dsouza, R., Müller-Werkmeister, H. M., Tellkamp, F., Miller, R. J. D. & Pai, E. F. (2019). *Science*, **365**, 1167–1170.
- Mora, E. de la, Coquelle, N., Bury, C. S., Rosenthal, M., Holton, J. M., Carmichael, I., Garman, E. F., Burghammer, M., Colletier, J.-P. & Weik, M. (2020). *Proc. Natl Acad. Sci.* **117**, 4142–4151.
- Murray, J. W., Garman, E. F. & Ravelli, R. B. G. (2004). *J. Appl. Cryst.* **37**, 513–522.
- Murray, T. D., Lyubimov, A. Y., Ogata, C. M., Vo, H., Uervirojnangkoorn, M., Brunger, A. T. & Berger, J. M. (2015). *Acta Cryst.* **D71**, 1987–1997.
- Murshudov, G. N., Skubák, P., Lebedev, A. A., Pannu, N. S., Steiner, R. A., Nicholls, R. A., Winn, M. D., Long, F. & Vagin, A. A. (2011). *Acta Cryst.* **D67**, 355–367.
- Nanao, M. H., Sheldrick, G. M. & Ravelli, R. B. G. (2005). *Acta Cryst.* **D61**, 1227–1237.
- Nave, C. & Garman, E. F. (2005). *J. Synchrotron Rad.* **12**, 257–260.
- Nogly, P., James, D., Wang, D., White, T. A., Zatsepin, N., Shilova, A., Nelson, G., Liu, H., Johansson, L., Heymann, M., Jaeger, K., Metz, M., Wickstrand, C., Wu, W., Båth, P., Berntsen, P., Oberthuer, D., Panneels, V., Cherezov, V., Chapman, H., Schertler, G., Neutze, R., Spence, J., Moraes, I., Burghammer, M., Standfuss, J. & Weierstall, U. (2015). *IUCrJ*, **2**, 168–176.
- Petterson, E. F., Goddard, T. D., Huang, C. C., Couch, G. S., Greenblatt, D. M., Meng, E. C. & Ferrin, T. E. (2004). *J. Comput. Chem.* **25**, 1605–1612.
- Powell, H. R., Johnson, O. & Leslie, A. G. W. (2013). *Acta Cryst.* **D69**, 1195–1203.
- Roedig, P., Vartiainen, I., Duman, R., Panneerselvam, S., Stübe, N., Lorbeer, O., Warmer, M., Sutton, G., Stuart, D. I., Weckert, E., David, C., Wagner, A. & Meents, A. (2015). *Sci. Rep.* **5**, 10451.
- Sadqi, M., Casares, S., Abril, M. A., López-Mayorga, O., Conejero-Lara, F. & Freire, E. (1999). *Biochemistry*, **38**, 8899–8906.
- Sauter, C., Otálora, F., Gavira, J.-A., Vidal, O., Giegé, R. & García-Ruiz, J. M. (2001). *Acta Cryst.* **D57**, 1119–1126.
- Schulz, E. C., Mehrabi, P., Müller-Werkmeister, H. M., Tellkamp, F., Jha, A., Stuart, W., Persch, E., De Gasparo, R., Diederich, F., Pai, E. F. & Miller, R. J. D. (2018). *Nat. Methods*, **15**, 901–904.
- Shelley, K. L., Dixon, T. P. E., Brooks-Bartlett, J. C. & Garman, E. F. (2018). *J. Appl. Cryst.* **51**, 552–559.
- Smith, G. D. & Blessing, R. H. (2003). *Acta Cryst.* **D59**, 1384–1394.
- Sutton, K. A., Black, P. J., Mercer, K. R., Garman, E. F., Owen, R. L., Snell, E. H. & Bernhard, W. A. (2013). *Acta Cryst.* **D69**, 2381–2394.
- Vagin, A. & Teplyakov, A. (2010). *Acta Cryst.* **D66**, 22–25.
- Weierstall, U., James, D., Wang, C., White, T. A., Wang, D., Liu, W., Spence, J. C. H., Bruce Doak, R., Nelson, G., Fromme, P., Fromme, R., Grotjohann, I., Kupitz, C., Zatsepin, N. A., Liu, H., Basu, S., Wacker, D., Won Han, G., Katritch, V., Boutet, S., Messerschmidt, M., Williams, G. J., Koglin, J. E., Marvin Seibert, M., Klinker, M., Gati, C., Shoeman, R. L., Barty, A., Chapman, H. N., Kirian, R. A., Beyerlein, K. R., Stevens, R. C., Li, D., Shah, S. T. A., Howe, N., Caffrey, M. & Cherezov, V. (2014). *Nat. Commun.* **5**, 3309.
- Weik, M., Ravelli, R. B. G., Kryger, G., McSweeney, S., Raves, M. L., Harel, M., Gros, P., Silman, I., Kroon, J. & Sussman, J. L. (2000). *Proc. Natl Acad. Sci. USA*, **97**, 623–628.
- White, T. A. (2019). *Acta Cryst.* **D75**, 219–233.
- White, T. A., Kirian, R. A., Martin, A. V., Aquila, A., Nass, K., Barty, A. & Chapman, H. N. (2012). *J. Appl. Cryst.* **45**, 335–341.
- Wiedorn, M. O., Oberthür, D., Bean, R., Schubert, R., Werner, N., Abbey, B., Aepfelbacher, M., Adriano, L., Allahgholi, A., Al-Qudami, N., Andreasson, J., Aplin, S., Awel, S., Ayyer, K., Bajt, S., Barák, I., Bari, S., Bielecki, J., Botha, S., Boukhelef, D., Brehm, W., Brockhauser, S., Cheviakov, I., Coleman, M. A., Cruz-Mazo, F., Danilevski, C., Darmanin, C., Doak, R. B., Domaracky, M., Dörner, K., Du, Y., Fangohr, H., Fleckenstein, H., Frank, M., Fromme, P., Gañán-Calvo, A. M., Gevorkov, Y., Giewekemeyer, K., Ginn, H. M., Graafsma, H., Graceffa, R., Greiffenberg, D., Gumprecht, L., Göttlicher, P., Hajdu, J., Hauf, S., Heymann, M., Holmes, S., Horke, D. A., Hunter, M. S., Imlau, S., Kaukher, A., Kim, Y., Klyuev, A., Knoška, J., Kobe, B., Kuhn, M., Kupitz, C., Küpper, J., Lahey-Rudolph, J. M., Laurus, T., Le Cong, K., Letrun, R., Xavier, P. L., Maia, L., Maia, F. R. N. C., Mariani, V., Messerschmidt, M., Metz, M., Mezza, D., Michelat, T., Mills, G., Monteiro, D. C. F., Morgan, A., Mühlig, K., Munke, A., Münnich, A., Nette, J., Nugent, K. A., Nuguid, T., Orville, A. M., Pandey, S., Pena, G., Villanueva-Perez, P., Poehlsen, J., Previtali, G., Redecke, L., Riekehr, W. M., Rohde, H., Round, A., Safenreiter, T., Sarrou, I., Sato, T., Schmidt, M., Schmitt, B., Schönherr, R., Schulz, J., Sellberg, J. A., Seibert, M. M., Seuring, C., Shelby, M. L., Shoeman, R. L., Sikorski, M., Silenzi, A., Stan, C. A., Shi, X., Stern, S., Sztuk-Dambietz, J., Szuba, J., Tolstikova, A., Trebbin, M., Trunk, U., Vagovic, P., Ve, T., Weinhausen, B., White, T. A., Wrona, K., Xu, C., Yefanov, O., Zatsepin, N., Zhang, J., Perbandt, M., Mancuso, A. P., Betzel, C., Chapman, H. & Barty, A. (2018). *Nat. Commun.* **9**, 4025.
- Winn, M. D., Ballard, C. C., Cowtan, K. D., Dodson, E. J., Emsley, P., Evans, P. R., Keegan, R. M., Krissinel, E. B., Leslie, A. G. W., McCoy, A., McNicholas, S. J., Murshudov, G. N., Pannu, N. S., Potterton, E. A., Powell, H. R., Read, R. J., Vagin, A. & Wilson, K. S. (2011). *Acta Cryst.* **D67**, 235–242.
- Zeldin, O. B., Brockhauser, S., Bremridge, J., Holton, J. M. & Garman, E. F. (2013). *Proc. Natl Acad. Sci. USA*, **110**, 20551–20556.